Check for updates

AGU ADVANCING EARTH AND SPACE SCIENCE

Water Resources Research

RESEARCH ARTICLE
10.1029/2020WR029460

Preferential Solute Transport in Low Permeability Zones During Spontaneous Imbibition in Heterogeneous Porous Media

Christopher Zahasky[1] **and Sally M. Benson**[2]

[1]Department of Geoscience, University of Wisconsin-Madison, Madison, WI, USA, [2]Department of Energy Resources Engineering, Stanford University, Stanford, CA, USA

Key Points:

- Positron emission tomography elucidates solute transport behavior during spontaneous imbibition in heterogeneous porous media
- In the presence of solute concentration gradients, solute is advected into low permeability zones during spontaneous imbibition
- Solute advection into low permeability zones during imbibition is greater with stronger permeability heterogeneity

Correspondence to:
C. Zahasky,
czahasky@wisc.edu

Citation:
Zahasky, C., & Benson, S. M. (2022). Preferential solute transport in low permeability zones during spontaneous imbibition in heterogeneous porous media. *Water Resources Research*, *58*, e2020WR029460. https://doi.org/10.1029/2020WR029460

Received 15 DEC 2020
Accepted 7 JAN 2022

Author Contributions:
Conceptualization: Christopher Zahasky
Formal analysis: Christopher Zahasky
Funding acquisition: Sally M. Benson
Investigation: Christopher Zahasky
Methodology: Christopher Zahasky
Resources: Sally M. Benson
Visualization: Christopher Zahasky
Writing – original draft: Christopher Zahasky
Writing – review & editing: Christopher Zahasky, Sally M. Benson

© 2022. American Geophysical Union. All Rights Reserved.

Abstract Multiphase flows in porous media, and the associated solute transport processes, are controlled by a combination of gravity, capillary, and viscous forces. Geologic heterogeneity influences flow and transport processes, yet gaps exist in our understanding of how heterogeneity impacts capillary-driven transport, such as during spontaneous imbibition. Here we use positron emission tomography, combined with a newly developed method for conducting spontaneous imbibition experiments, to observe solute transport into low permeability regions during imbibition. Using an experimentally parameterized 2D numerical model, we demonstrate how capillary-driven flow near the imbibition front can carry solutes into low permeability regions. This process displaces solutes from high permeability zones, while the cumulative amount of solute in low permeability zones increases, opposite of what is observed under fully saturated solute transport conditions. These results highlight the complex flow and solute transport behavior that arise during multiphase displacements in heterogeneous geologic porous media.

Plain Language Summary Solutes and contaminants dissolved in a fluid, such as water, are carried along with the fluid as it migrates in the subsurface. In some subsurface settings, there are multiple fluids present. For example, above the water table a zone of soil and rock has pores filled with different fractions of water and air; in geologic carbon storage reservoirs the rock has pores filled with different fractions of supercritical CO_2 and brine. The nature of the geologic setting controls how these fluids displace one another in the subsurface. In this study, we perform experiments that are quantified with medical imaging techniques to study how solutes are carried with water during a specific type of displacement process known as spontaneous imbibition. These imaging techniques allow us to see inside geologic rock cores and monitor solute migration and immobilization processes. Results of the experiments and associated mathematical modeling highlight a mechanism of solute immobilization that is unique to the process of spontaneous imbibition. These results may help explain why some contaminants can be immobilized for extended periods of time before reaching groundwater supplies.

1. Introduction

Solute transport during multiphase fluid displacement is an incredibly complex yet ubiquitous phenomenon, controlling processes such as contaminant transport in the capillary fringe (Silliman et al., 2002), the transport of dissolved species in fractured geothermal reservoirs, and the evolution of aqueous chemical gradients in geologic carbon storage reservoirs. Spontaneous imbibition is a specific multiphase displacement process driven by capillary forces in a porous medium. These capillary forces arise from the pore-scale properties of a porous media such as pore geometry and local wetting conditions (Bartels et al., 2019). If a solute or dissolved species is present in the imbibing wetting fluid, the solute transport and mixing processes will be controlled by the capillary-driven flow field.

Heterogeneity is an inherent characteristic of geologic materials that is expressed as variability in porosity and permeability in single phase, fully saturated conditions (Koltermann & Gorelick, 1996). Under heterogeneous fully saturated conditions, conservative solutes are preferentially transported through higher permeability regions where there is lower resistance to flow and thus advective velocities are higher (Dogan et al., 2014). Solute transport into low permeability zones, where advective velocities are lower, is driven by a combination of advection, dispersion, and diffusion, depending on the strength and nature of the heterogeneity (Huang et al., 1995; Kurotori et al., 2019).

In addition to porosity and permeability heterogeneity, capillary heterogeneity can have a strong impact on multiphase flow under partially saturated conditions (Ross, 1990). Capillary heterogeneity describes the differences in capillary pressure characteristic curves and capillary entry pressure that are the result of spatial variations in pore size distribution throughout a porous media (Brooks & Corey, 1966; Zahasky et al., 2020). Field observations, experiments, and numerical models have highlighted the influence that capillary heterogeneity can have on multiphase displacement processes across spatial length scales (Debbabi et al., 2017; Jackson & Krevor, 2020; Li & Benson, 2015; Lu et al., 2020; Poulsen & Kueper, 1992; Ringrose et al., 1993; Schlüter et al., 2012). During spontaneous imbibition, capillary heterogeneity may destabilize the imbibition front due to more rapid imbibition into regions of a porous medium with higher capillary pressure. However, this is strongly coupled and potentially counteracted by the local effective permeability and corresponding viscous resistance to imbibition (Ashraf & Phirani, 2019).

Viscous forces, arising from the frictional resistance of flowing viscous fluids, may suppress capillary or gravity-driven fluid saturation variations during multiphase displacement processes. This viscous suppression in a porous medium occurs when there are larger pressure gradients in the upstream displacing fluid than in the less viscous fluid being displaced. This viscous suppression is more likely to occur when a higher viscosity fluid displaces a lower viscosity fluid (Homsy, 1987). The viscosity of water is approximately two orders of magnitude greater than the viscosity of air. In systems with water displacing gas, this viscosity contrast can generate viscous pressure gradients that may override gravitational forces and capillary heterogeneity, leading to uniform displacement fronts. The stability of interfaces resulting from a high-viscosity fluid displacing a less viscous fluid have been studied at a range of scales from microfluidics (Al-Housseiny et al., 2012; Rabbani et al., 2018) to rock cores (Zahasky & Benson, 2019; Zhao et al., 2017) and Hele-Shaw cells (Saffman & Taylor, 1958). For an extensive review of this process and mathematical details see (Homsy, 1987; Woods, 2014).

The water saturation distribution in unsaturated porous media is thus controlled by a complex balance of gravity and viscous forces and the capillary pressure characteristics of the porous media. Understanding the coupled multiphase and solute transport behavior under heterogeneous unsaturated conditions is key to describing processes such as contaminant migration through the unsaturated zone (Guo et al., 2019; Lyu et al., 2018; Weber et al., 2017), migration and partition of nonaqueous phase liquids in aquifers (McCarthy & Johnson, 1993; Werner & Höhener, 2002), and the evolution of aqueous chemical and brine gradients in geologic carbon storage reservoirs (Green & Ennis-King, 2010; MacMinn et al., 2012). Despite significant advances in descriptions of the multiphase behavior of these processes, major gaps exist around our understanding of coupled aqueous solute transport and multiphase processes in heterogeneous geologic systems (Berkowitz et al., 2004; Hasan et al., 2020; National Research Council, 2000).

In this study, we use positron emission tomography and X-ray computed tomography, combined with a recently developed method for conducting spontaneous imbibition experiments (Zahasky & Benson, 2019), to quantify the dynamic changes in solute concentration distribution in the aqueous wetting phase when driven entirely by capillary forces. These *in situ* imaging and experimental methods provide observations of the coupled processes of spontaneous imbibition and solute transport that have not been previously possible in geologic materials. A 2D numerical model is used to illustrate how imbibition-driven flow orthogonal to the direction of imbibition can lead to strong spatial variability in solute distributions across the imbibition front. Specifically, elevated solute concentrations in low permeability zones arise during spontaneous imbibition conditions, as opposed to preferential flow of solutes in high permeability zones observed during single phase solute transport.

2. Experimental Approach

2.1. Experimental and Imaging Methods

Two-end-open free spontaneous imbibition experiments were performed using the experimental method recently described in Zahasky and Benson (2019) to isolate and analyze the mechanism of capillary-driven solute transport. During these experiments, a 5.08 cm diameter by 10 cm long Berea sandstone core is loaded into a coreholder that enables a confining pressure, and thus no-flow conditions, to be applied to the cylindrical faces of the sample. Water is delivered to the inlet face of the sample and an additional fluid entry port at the inlet face of the coreholder is connected to the tubing from the outlet face of the coreholder. A schematic illustration of the experimental setup is shown at the top of Figure 1. The presence of this bypass tubing prevents a differential

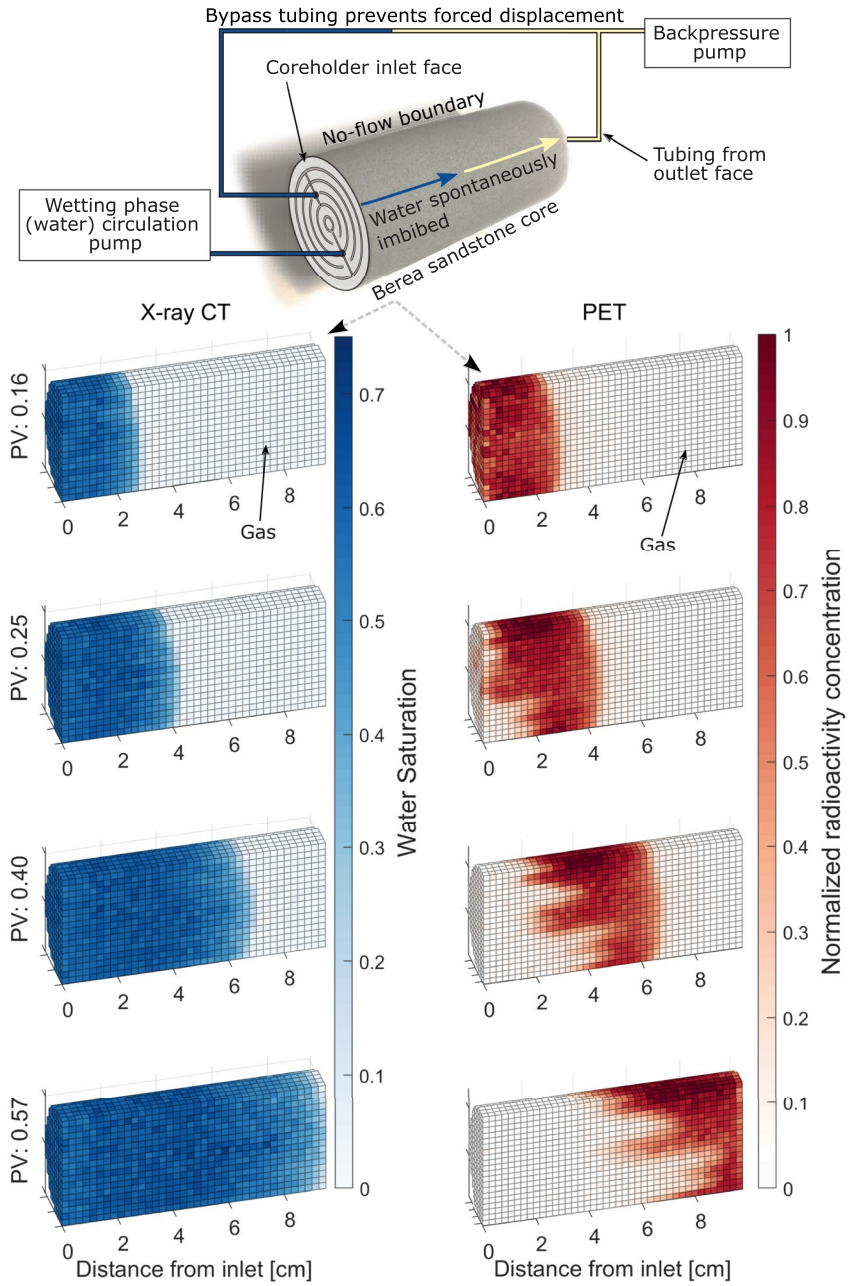

Figure 1. (Top) Illustration of experimental configuration overlaid on a photo of the Berea sandstone core used for this study. The inlet and outlet caps are in contact with the core sample. The plumbing setup is schematically shown for circulating water (indicated by the blue tubing) and recovering displaced gas phase (indicated by the yellow tubing) from the core. Blue and yellow arrows represent the wetting phase spontaneously imbibing and displacing the nonwetting gas phase, respectively. (Left column) Water saturation distributions measured in the core with X-ray CT. The imbibition progress is given in the fraction of pore volumes (PV) of fluid imbibed. (Right column) Plots showing PET-measured solute radiotracer concentration distribution during a repeated spontaneous imbibition experiment. The concentration distributions correspond to the identical pore volume imbibed and water saturation distribution in the corresponding row of the X-ray CT data. The voxel side length of the X-ray CT images is 2.5 mm and the voxel side length of the PET images is 2.3 mm.

pressure from being applied to the sample such that all fluid entering the core sample does so only by capillary forces, enabling the observation of the spontaneous imbibition process. The gas displaced during imbibition flows out of the core into a slightly pressurized (100 kPa) outlet tank that is nearly identical to the pressure in the water delivery pump. The fluid pair of water displacing gas was selected to mimic vadose zone conditions.

The porosity, permeability, relative permeability, and average capillary pressure curves of the Berea sandstone core used in these experiments has been previously characterized (Vasco et al., 2018; Zahasky & Benson, 2018, 2019). Results of single-phase, steady-state water injection in these studies measured a core-average permeability ($\bar{k}$) of 23 millidarcy (mD). The heterogeneous subcore permeability field has been estimated using a semi-analytical streamtube permeability analysis (Zahasky & Benson, 2018) as well as a three-dimensional numerical inversion method (Vasco et al., 2018). These studies found that the permeability varies throughout the sample by over a factor of 2, with a minimum near 10 mD and a maximum of ~30 mD. The subtle permeability structure is a result of the axial-parallel lamination that is visually present in the physical sample and in clinical X-ray computed tomography (X-ray CT) scans. Sample porosity was measured with multiple small plugs analyzed with a Micromeritics AccuPyc II Helium Pycnometer. The average porosity of seven small plugs was 0.204 with a standard deviation of 0.0068.

Two repeated primary imbibition experiments were performed for this study, one imaged with X-ray CT, and the other imaged with micro-positron emission tomography (PET). X-ray CT enables the quantification of changes in water saturation during spontaneous imbibition using classic CT linear scaling expressions (Akin & Kovscek, 2003). The repeated primary spontaneous imbibition experiment imaged with PET was performed under identical conditions except that the initial water imbibed contained the positron-emitting radiotracer Fludeoxyglucose (^{18}F-FDG). Positron emission tomography measures the 3D time-lapse radiotracer concentration in each voxel of the core during the imbibition processes. To ensure that the entire imbibition process was captured, the core was scanned for 6 hours in two three-hour scans.

After ~0.16 pore volumes (6.3 mL) of water with ^{18}F-FDG was spontaneously imbibed, the wetting phase fluid delivered to the inlet was switched to water with no radiotracer for the remainder of the imbibition experiment. This volume of water with radiotracer was determined during the experiment to optimize PET image quality. If too much radiotracer was added it would saturate the photon detectors in the PET scanner while too little tracer leads to less coincidence detection events and greater image noise (Zahasky et al., 2019). Zero-order spatial moment analysis was used to ensure accurate concatenation of the two three-hour scans. Once all of the available radiotracer was imbibed into the core the total amount of measured radiotracer in the core (i.e., the zero moment) varied by less than 10%. Additional details and methods of PET imaging for applications in earth science can be found in Zahasky et al. (2019) as well as additional verification and analysis of concentration measurement accuracy (Kurotori et al., 2019, 2020; Zahasky & Benson, 2018).

2.2. Experimental Results of Solute Transport During Spontaneous Imbibition

The left column of plots in Figure 1 illustrates the piston-like displacement of water spontaneously imbibing into the horizontally oriented core. The imbibition front evolves as $t^{-1/2}$, in agreement with the Lucas-Washburn equation (Washburn, 1921) for capillary-driven flow as shown in the left plot in Figure 2. This decrease in imbibition rate is due to the increasing viscous resistance experienced by water as it imbibes, increasing the distance between the source of water at the inlet of the sample and the imbibition front. The overall imbibition rate in these experiments is independent of gravitational forces due to the horizontal orientation of the core.

The water saturation is uniform in the region behind the front, even though the permeability of the laminations varies by over a factor of 2 as shown in the upper right plot in Figure 2 and described in the following section. The front stability is a result of the viscous pressure gradient in the water, resulting from water displacement established by capillary forces pulling water from the inlet of the core to the imbibition front, that is, orders of magnitude higher than the pressure gradient in the displaced low-viscosity gas. These viscous forces thus limit the imbibition front roughness and minimize gravity-induced inclination. This type of piston-like displacement is commonly observed in imbibition experiments with water displacing gas and in-situ saturation monitoring (Alyafei et al., 2016; Gruener et al., 2012; Zhao et al., 2017).

Despite the nearly uniform saturation front measured with X-ray CT, the PET images on the right side of Figure 1 highlight the complex solute advection behavior behind the spontaneous imbibition front. These results are fundamentally different from solute transport under saturated conditions. Under saturated conditions, if the hydraulic gradient is parallel to laminations with different permeability, then the solute advection rates will occur proportional to layer permeability with no component of orthogonal transport except transverse hydrodynamic dispersion. Under spontaneous imbibition conditions, we observe a strong component of flow orthogonal to the

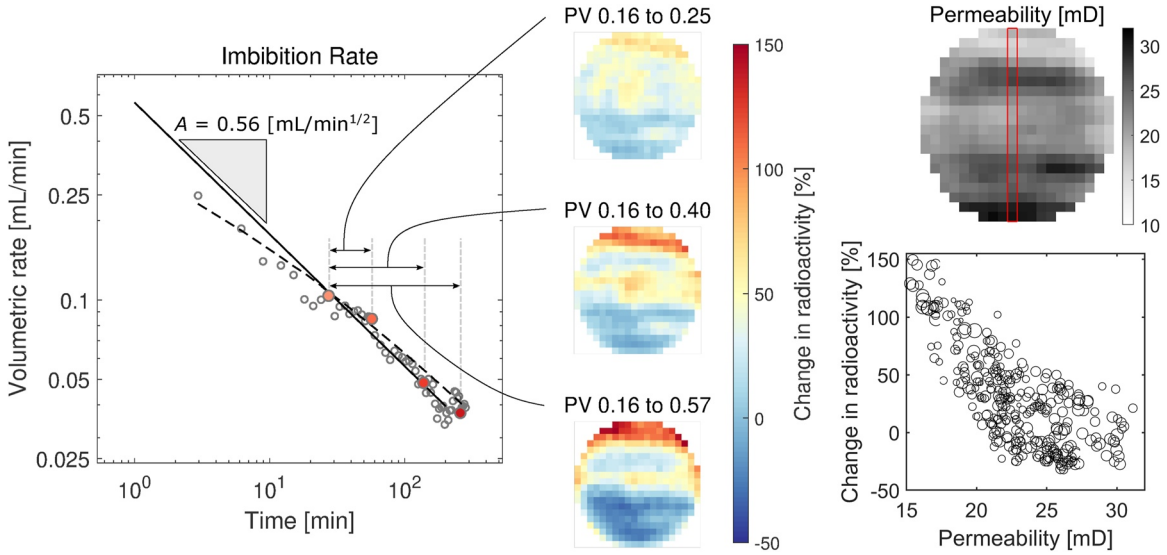

Figure 2. (Left plot) Water imbibition rate as a function of time as measured from repeated X-ray CT scans during the spontaneous imbibition experiment. The colored points from light to dark red correspond to the imbibition times of PV = 0.16, 0.25, 0.40, and 0.57, respectively. The imbibition rate can be described with characteristic $t^{-1/2}$ scaling with $Q^w_{imb} = At^{-1/2}$ as described by McWhorter and Sunada (1990). The dashed black line is the cumulative imbibition rate of the TOUGH2 model described in Section 5. (Center plots) Change in radiotracer mass calculated by summing the radiotracer mass along the long axis of the core. This highlights changes in activity orthogonal to the direction of spontaneous imbibition, looking down the long axis of the core from the inlet. The percent change is calculated relative to the first frame shown in Figure 1 at a pore volume (PV) of water imbibed of 0.16. The percent change in the top, middle, and lower-left plots is calculated between the first frame (PV = 0.16) and the second (PV = 0.25), third (PV = 0.4), and fourth (PV = 0.57) frames shown in Figure 1, respectively. (Upper right plot) Approximation of permeability, in millidarcy, averaged along the axis of the core using the experimental and analytical methods described in Zahasky and Benson (2018). The red rectangle indicates the axial-parallel permeability map used for the modeling analysis in Section 5. (Lower right plot) Cross-plot highlighting the negative correlation between change in radioactivity, between PV = 0.16 and PV = 0.57, as a function of permeability. The size of the points are approximately equal to the standard error between five different single-phase experiments used to approximate the permeability.

direction of imbibition. This orthogonal flow in the imbibition front carries solutes from the high permeability layers into the low permeability layers, resulting in large spatial variations in radiotracer concentration at the conclusion of the spontaneous imbibition process.

2.3. Relationship Between Radiotracer Concentration Distribution and Subcore Permeability

Analysis of the solute distributions highlights regions where cumulative radiotracer increases and where radiotracer concentration decreases throughout the spontaneous imbibition process. The orthogonal flow in the imbibition front can be quantified by changes in total radiotracer contained in rows of voxels parallel to the axis core, as determined by the sum of radiotracer mass along these rows of voxels. The center column of plots in Figure 2 highlight areas of radiotracer accumulation as indicated by a positive change in radiotracer mass (warmer colored areas). The cooler colored areas indicate areas with decreasing radiotracer mass. The permeability distribution in the core sample is shown in the upper right plot in Figure 2. This permeability is equivalent to the harmonically averaged permeability along the long axis of the core, in corresponding regions to the radiotracer mass calculations. The permeability was approximated using the moment-based semi-analytical method from single phase flow experiments described in Zahasky and Benson (2018). Permeability averaged along the axis of the core is a good approximation of the permeability structure of this sample due to the axial-parallel lamination of the sandstone sample. The lower right plot in Figure 2 is a cross plot of the change in radioactivity in each row of voxels along the axis of the core from 0.16 PV of water imbibed to 0.57 PV of water imbibed, the same data illustrated in the bottom-center plot, as a function of permeability in corresponding spatial regions of the core sample. The results in Figure 2 clearly show that the radiotracer is accumulating in low permeability portions of the core and decreasing in the high permeability portions of the core.

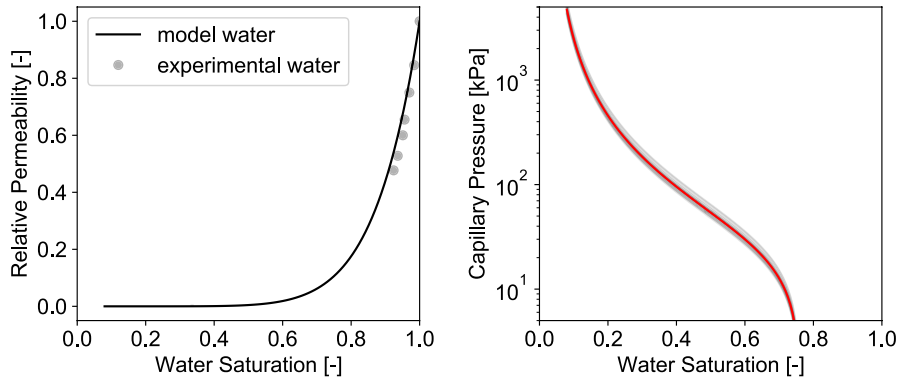

Figure 3. (Left) Water relative permeability of the TOUGH2 imbibition model (black line). The gray circles indicate core-average water relative permeability measured during a drainage experiment previously reported in Zahasky and Benson (2019). The experimental marker size is proportional to relative permeability measurement error, specifically two standard deviations of measurement noise. (Right) Core-average capillary pressure curve (red line) determined from a combination of mercury intrusion capillary pressure measurements (MICP) and 1D numerical capillary pressure calculations using the method of Zahasky and Benson (2019). The faint black lines are the scaled capillary pressure curves based on the streamtube permeability using the Levertt-J capillary scaling methods (Alyafei & Blunt, 2018; Leverett, 1940; Tokunaga et al., 2013).

3. Numerical Modeling of Local Fluid Flow During Spontaneous Imbibition

To further investigate the influence of heterogeneity on spontaneous imbibition, we used TOUGH2 with the EOS3 equation of state (Pruess & Moridis, 2012) to model a system analogous to the one used for the experiments. The spontaneous imbibition process was modeled with EOS3 solving for gas/water saturation, fluid pressure, temperature, and air mass fraction as a function of time.

The problem was first simplified to a two-dimensional model with an intrinsic permeability field that only varies in the direction orthogonal to the direction of imbibition and a homogeneous porosity equal to the core-average value. This simplification was done for several reasons. In two dimensions it is possible to clearly illustrate the impact of heterogeneity on fluid flow conditions without considering the influence of out-of-plane impacts. Second, the method for heterogeneous permeability inversion is only a semi-analytical approximation. Without a highly resolved 3D permeability field, and spatially resolved description of capillary heterogeneity, experiment-model comparisons are limited due to the strong influence on imbibition-driven transport process. Finally, the simplified 2D layered permeability field allows for a clear analysis of the mechanism and impact of flow orthogonal to the direction of imbibition. This enables an analysis of how the orthogonal flow rates change as imbibition progresses and the total imbibition rate slows. The model width was set to maintain an equivalent cross-sectional area so that the model can be constrained by the cumulative imbibition rate illustrated in the left plot in Figure 2. The values used for the vertically varying intrinsic permeability field are highlighted by the red box in the upper-right plot in Figure 2.

The multiphase characteristic curves used in the model are plotted in Figure 3. The red line in the right plot in Figure 3 illustrates the core-average van Genuchten capillary pressure curve (TOUGH2 parameter ICP = 7) determined from a combination of mercury intrusion capillary pressure measurements (MICP) and 1D numerical capillary pressure calculations using the method of Zahasky and Benson (2019). The van Genuchten parameters were $\lambda = 0.345$, $S_{wr} = 0.03$, $S_{gr} = 1–0.76 = 0.24$, core-average capillary entry pressure ($\bar{P}_0$) of 29 kPa, and maximum capillary pressure of 5,000 kPa. The faint black lines are the scaled capillary pressure curves used in each layer of the model using the Levertt-J capillary scaling based on the layer permeability (Alyafei & Blunt, 2018; Leverett, 1940; Tokunaga et al., 2013).

The water relative permeability function was approximated by fitting a power law relative permeability function (TOUGH2 parameter IRP = 2, $k_{rw} = S_w^{7.8}$) to the core-average water relative permeability measured during a drainage experiment previously reported in Zahasky and Benson (2019). The exponent was adjusted slightly to align the model core-average imbibition rate, shown by the dashed black line in the left plot in Figure 2, with the experimentally measured bulk imbibition rate. In this relative permeability model, the gas relative permeability

in every cell was set to one and was independent of water saturation changes. This model thus ignores gas-phase mobility reduction and is valid due to the very slow cocurrent imbibition rates and because the viscosity of nitrogen gas is several orders of magnitude lower than water.

The model geometry, input file generation, and model output analysis were performed using PyTOUGH (Florian Wellmann et al., 2012). The cocurrent two-end-open free spontaneous imbibition process requires a constant water saturation equal to one and zero at the inlet and outlet, respectively. These Dirichlet conditions prescribing fixed thermodynamic conditions were implemented in TOUGH2 by assigning very large volumes (500 m^3) to the grid cells adjacent to the inlet and outlet of the core. This creates a very large reservoir of water at the inlet of the core that can spontaneously imbibe into the core, and a reservoir of gas at the outlet of the core for the displaced gas to escape. The initial pressure conditions in every grid cell in the model were set to 103 kPa (1 atm). An initial water saturation of approximately zero ($S_{wi} = 1 \times 10^{-6}$) was assigned to every grid cell except the inlet grid cell. The inlet grid cell reservoir had an initial water saturation of 1. Upon simulation initiation, the large capillary pressure gradient resulting from the water saturation gradient drives the spontaneous imbibition flow process.

The extremely high capillary-driven pressure gradients during spontaneous imbibition require careful attention to model grid definition and often require very fine model discretization in the direction of imbibition (Khan et al., 2018; Pooladi-Darvish & Firoozabadi, 2000). To determine the optimal grid discretization, a 1D grid refinement study was performed and is described in Appendix A. Based on the grid refinement study, the model grid was set to 1,200 cells in the direction of imbibition (termed the x-direction) and 20 cells in the vertical direction (termed the z-direction and parallel to gravity). This results in a grid cell size of 0.08 mm in the x-direction and 2.5 mm in the z-direction. The model grid was oriented such that the imbibition proceeded horizontally, identical to the experimental conditions, and gravitational forces were not neglected. The TOUGH2 input and output files, PyTOUGH scripts used to generate the input files are available in the data repository linked in the Acknowledgments.

The modeled water saturation results at times identical to those in the experiments shown in Figure 1 are plotted in the left column of plots in Figure 4. The model-average imbibition rate is quantitatively compared with the experimentally measured imbibition rates in the right plot of Figure 2 as indicated by the dashed line and scatter points, respectively. These plots indicate that the model closely captures the timing and spontaneous imbibition process that was observed experimentally. These results also show how the viscous stability of the imbibition front present in the X-ray CT images in Figure 1 is also captured by the numerical model.

The grid cell-averaged spontaneous imbibition-driven flow rate results are overlaid on the two-dimensional intrinsic permeability field in the right column of plots in Figure 4. These results highlight the striking influence of permeability heterogeneity on fluid flow, and thus advective behavior of solutes, during spontaneous imbibition. Behind the imbibition front, where the water saturation has approximately reached the residual gas saturation, water and solutes are pulled into and through the higher permeability zones (darker gray layers) at a faster rate than the lower permeability zones (lighter gray layers). This preferential flow is illustrated by the (mostly green) arrows pointed toward the higher permeability zones at the inlet of the model. However as water approaches the imbibition front, there is a significant component of orthogonal flow to maintain the consistent saturation gradient across the imbibition front. This pattern is highlighted in the right plots of Figure 4 by the (mostly red) arrows pointing from the high permeability zones to lower permeability zones in the region around the imbibition front. This fluid flow pattern explains the mechanism responsible for producing PET imaging results that show solute accumulation in the low permeability zones of the core during spontaneous imbibition.

The results in Figure 4 also suggest that this effect is stronger in areas of higher heterogeneity. Specifically, the top region of the numerical model has the highest contrast in permeability and also experiences the largest magnitudes of flow orthogonal to the direction of imbibition, as indicated by the longest and darkest red arrows. The lower region of the model has more subtle heterogeneity and therefore slightly lower magnitudes of flow orthogonal to the direction of imbibition. The trend of higher permeability in the bottom of the model and lower permeability in the top of the model also leads to much more upward advection (red vectors) than downward advection (green vectors). This is in strong agreement with the results from Figure 2 that show a general migration in total solute mass from the bottom of the core to the top of the core throughout of the spontaneous imbibition process.

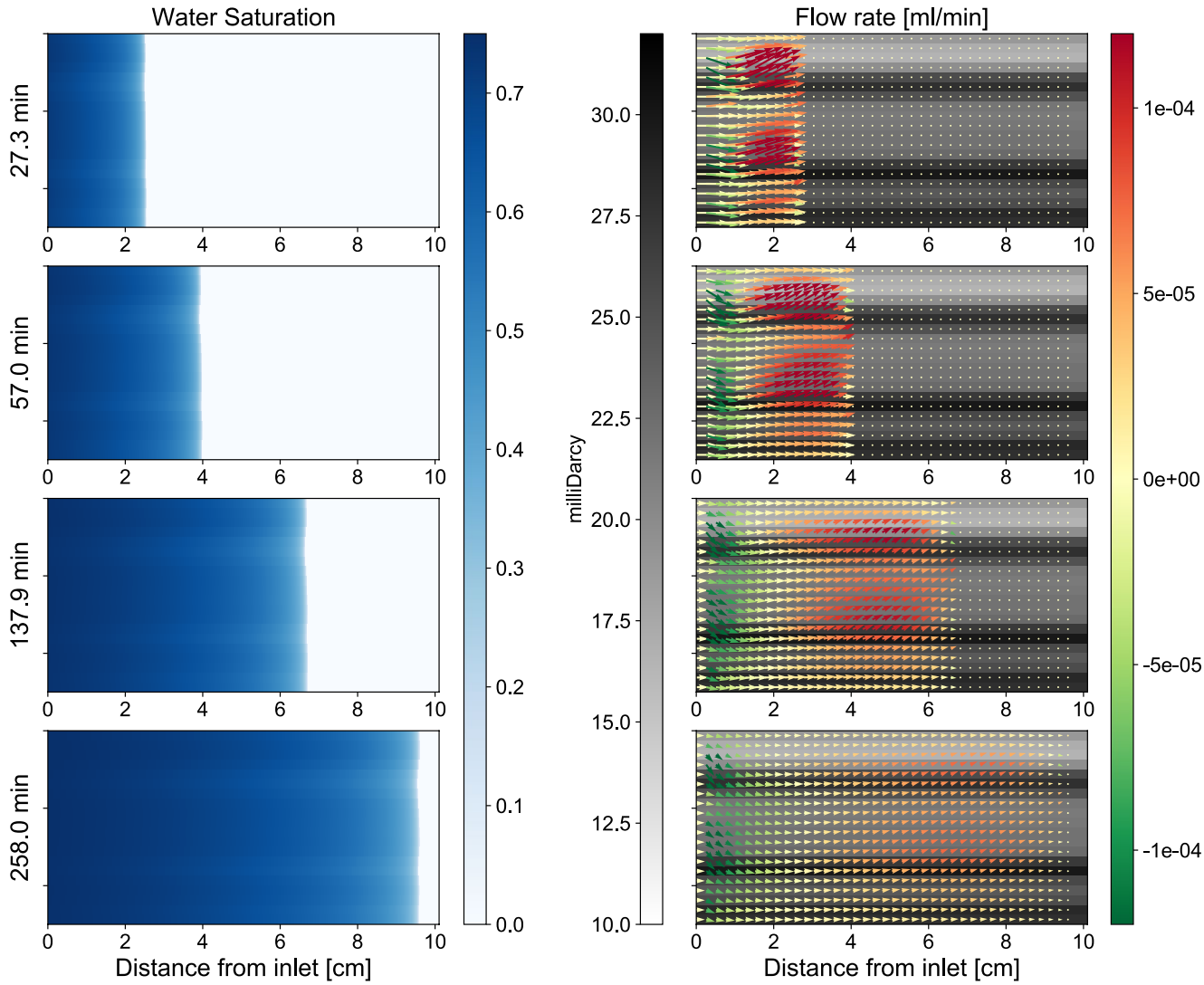

Figure 4. (Left column) Modeled water saturation distribution at times corresponding to the X-ray CT water saturation measurements shown in Figure 1 (PV:0.16 = 27.3 min, PV:0.25 = 57.0 min, PV:0.40 = 137.9 min, PV:0.57 = 258 min). (Right column) Two-dimensional intrinsic permeability fields along the axis of the core overlaid by the grid cell-average spontaneous imbibition-driven flow rate (FLO[LIQ] data from the TOUGH2 output converted to volumetric units). The vertical flow was multiplied by a factor of 30 to correct for the aspect ratio of the grid cells (dz/dx = 29.70). The flow rate in the vertical direction was then multiplied by a factor of 10 to emphasize the role of the advective velocity orthogonal to the direction of imbibition. The vector colors correspond to the flow rate component in the z-direction, orthogonal to the direction of imbibition. The green vectors indicate downward flow, while the red colors indicate an upward flow. A vector with a near-zero flow rate component in the z-direction appears yellow. The dots ahead of the imbibition front are zero flow rate vectors.

4. Numerical Modeling of Spontaneous Imbibition in More Heterogeneous Systems

To further validate the observations of the relative contributions of permeability heterogeneity and capillary heterogeneity on the spontaneous imbibition process, two additional models were constructed. In the first model, the permeability variation is exaggerated by a factor of 3, while keeping the mean model permeability constant. Specifically, each horizontal layer with a permeability k_i in the original model is replaced by a permeability of $k_{i\epsilon}$ with the following transform $k_{i\epsilon} = 3k_i - 2\bar{k}$, where $\bar{k}$ is the mean permeability. The mean permeability, grid cell characteristic curves, and all other model parameters are identical to the model presented in Section 5. The results of the model with exaggerated permeability heterogeneity are shown in Figure 5.

These model results emphasize several important flow observations during spontaneous imbibition. The saturation maps in the left column of plots in Figure 5 illustrate how gravity forces play a larger roll in the shape or slope of the imbibition front as the horizontal viscous pressure gradients exhibit greater variation in proportion to

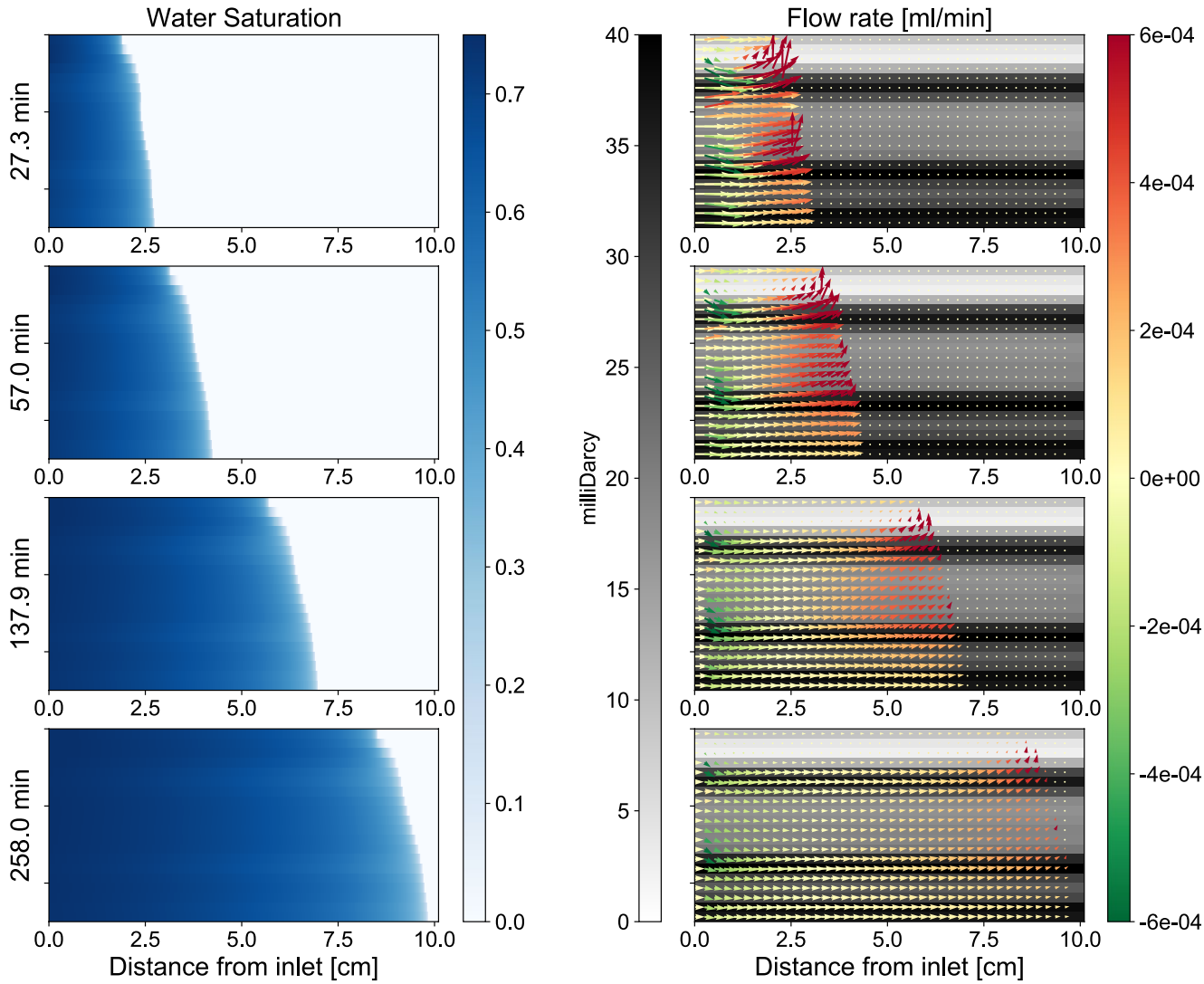

Figure 5. Model results showing the impact of three times larger permeability distribution on the spontaneous imbibition saturation and flow field distributions. The core-average permeability, grid cell characteristic curves, and all other model parameters are identical to those shown in Figure 4. (Left column) Modeled water saturation distribution at timesteps corresponding to model shown in Figure 4; 27.3, 57.0, 138, and 258 min from top to bottom, respectively. (Right column) Two-dimensional intrinsic permeability fields along the axis of the core overlaid by the grid cell-average spontaneous imbibition-driven flow rate (FLO[LIQ] data from the TOUGH2 output converted to volumetric units). The vertical flow was multiplied by a factor of 30 to correct for the aspect ratio of the grid cells (dz/dx = 29.70). The flow rate in the vertical direction was then multiplied by a factor of 2 to emphasize the role of the advective velocity orthogonal to the direction of imbibition. The vector colors correspond to the flow rate component in the z-direction, orthogonal to the direction of imbibition. The green vectors indicate downward flow while the red colors indicate an upward flow. Note that the maximum and minimum flow rate colorscale is a factor of 5 greater than Figure 4.

layer permeability. The flow rate distributions shown in the right column of plots in Figure 5 further demonstrate that higher contrast in permeability drive greater magnitudes of flow orthogonal to the direction of imbibition. At the entrance of the core the water is preferentially pulled into the high permeability layers. Near the imbibition front, there is significantly greater flow orthogonal to the direction of imbibition from high permeability to low permeability regions than in the base model presented in Figure 4.

In the second model, the capillary heterogeneity is exaggerated while the permeability remains identical to the model presented in Section 5. The capillary heterogeneity is exaggerated by performing the Levertt-J capillary scaling based on the transformed layer permeability $k_{i\epsilon}$ rather than the original permeability k_i. The wider variation in capillary heterogeneity is illustrated by plotting all of the capillary pressure curves for this model in Figure B1 in Appendix B. The grid cell permeability, core-average capillary pressure curve, relative permeability

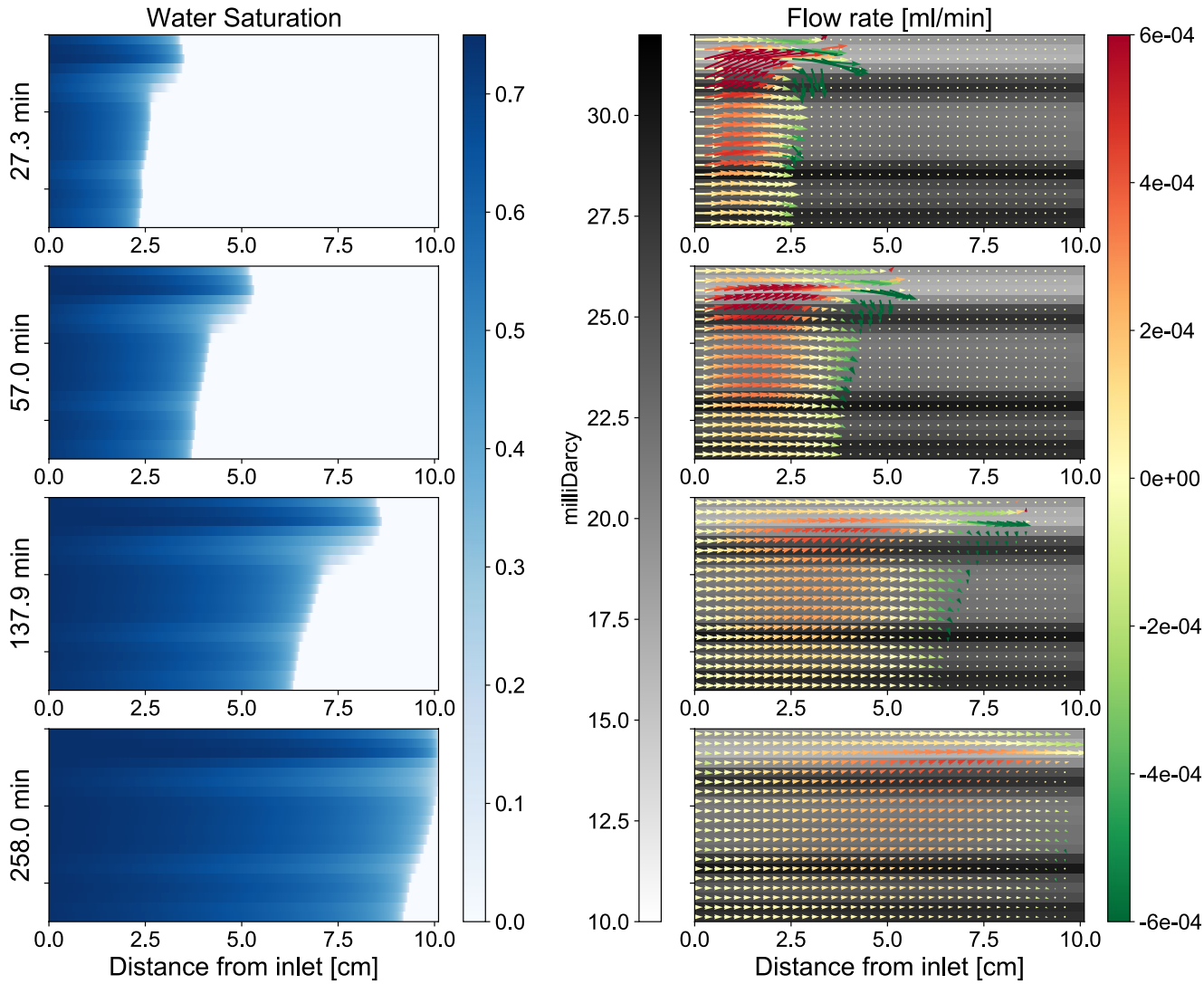

Figure 6. Model results showing the impact of larger capillary heterogeneity on the spontaneous imbibition saturation and flow field distributions. The grid cell permeability, core-average characteristic curves, and all other model parameters are identical to those shown in Figure 4. The capillary pressure curves used in this model are plotted in Figure B1 in Appendix B. (Left column) Modeled water saturation distribution at timesteps corresponding to model shown in Figure 4; 27.3, 57.0, 138, and 258 min from top to bottom, respectively. (Right column) Two-dimensional intrinsic permeability fields along the axis of the core overlaid by the grid cell-average spontaneous imbibition-driven flow rate (FLO[LIQ] data from the TOUGH2 output converted to volumetric units). The vertical flow was multiplied by a factor of 30 to correct for the aspect ratio of the grid cells (dz/dx = 29.70). The flow rate in the vertical direction was then multiplied by a factor of 2 to emphasize the role of the advective velocity orthogonal to the direction of imbibition. Note that the flow rate colorscale is a factor of 5 greater than Figure 4, identical to the colorscale in Figure 5.

curves, and all other model parameters are identical to the original model shown in Figure 4. The results of this model with exaggerated capillary heterogeneity are shown in Figure 6.

Results of the model dominated by capillary heterogeneity illustrate dramatically different flow behavior during spontaneous imbibition. In the water saturation distributions illustrated in the left column of plots in Figure 6, the capillary heterogeneity is so strong that it destabilizes the imbibition front. This is demonstrated by the more rapid rate of imbibition in the layers with higher capillary pressure characteristics, corresponding to the layers with lowest permeability. As a result, the local flow rate distributions in the right column of plots in Figure 6 show a completely different behavior relative to the previous models. Rather than water being preferentially pulled through high permeability layers to reach the imbibition front, the water is preferentially pulled through the layers with the lowest permeability and highest capillary pressure. Near the imbibition front the water, flows from these low permeability layers to high permeability layers, opposite of the behavior in the previous models.

Note that the magnitude of the orthogonal flow is similar to the model with stronger permeability heterogeneity, as indicated by identical colorbar ranges, however the spatial locations of upward and downward flow is reversed. Under flow conditions dominated by stronger capillary heterogeneity, solute would be expected to accumulate in the high permeability zones of the imbibition front rather than the low permeability zones.

5. Discussion and Implications

Results of the PET and X-ray CT imaging of spontaneous imbibition experiments and numerical modeling of local fluid flow show that the transport of solutes orthogonal to the direction of imbibition is driven by a combination of viscous, gravity, and capillary forces in heterogeneous rocks. In the spontaneous imbibition experiments performed in this study, a relatively stable piston-like imbibition front pulls water through the inlet and along the core displacing air. Away from the imbibition front, water is pulled at higher rates through the higher permeability portions of the rock. Near the imbibition front, water flows into the lower permeability portions of the rock to maintain the stable water saturation front. This component of flow orthogonal to the direction of imbibition decreases the mass of solute in the high permeability layers while increasing the cumulative amount of solute in the lower permeability regions of the core. This orthogonal flow into low permeability zones is distinctly different from preferential flow into higher permeability zones in a heterogeneous system under steady-state hydraulic gradients.

In the core used for the spontaneous imbibition experiments, the core permeability varies by less than a factor of 3. Despite this relatively subtle heterogeneity, the cumulative contribution of solute transport orthogonal to the direction of imbibition led to more than a two-fold increase in solute distributed in the lower permeability zone in the upper portion of the core. Corresponding simulation models illustrate that increased permeability heterogeneity significantly magnifies this effect while strong capillary heterogeneity can suppress this effect. These results highlight the need for multiscale capillary heterogeneity characterization (Pini et al., 2012), and the need for robust spatially resolved permeability inversion methods to accurately model three dimensional solute transport that occurs during coupled multiphase flow and transport processes.

This work has important implications for understanding solute transport during capillary-driven flow under multiphase flow conditions. While the experiments can only be imaged horizontally due to the geometry of the imaging systems, the results are applicable when capillary-driven displacement occurs in the presence of solute gradients. Examples of this type of capillary driven displacement include horizontal spontaneous imbibition from fractures, macropores, and other "fast paths" during infiltration or other multiphase displacement processes. Additional modeling approaches and multiscale experiments are required to further understand the short and long-term impacts of this complexly interconnected multiphase displacement and solute transport process.

Appendix A: Grid Refinement Study

To determine the optimal grid discretization for modeling the cocurrent spontaneous imbibition process, a 1D grid refinement study was performed. The model parameters are identical to those described in Section 5 except that the model is 1D with a homogeneous permeability of 23 mD and a single capillary pressure curve (red line in Figure 3). The model was run with a fixed domain size equal to the core (10 cm long and a cross-sectional area equal to 20.26 cm^2). The number of grid cells along the length of the core was initial set to 50 (dx = 0.2 cm) and increased by 50 up to 1,600 cells (dx = 0.006 25 cm). To assess the impact of model discretization, the imbibition front location after 120 min was recorded. The front location as a function of grid cell size increased dramatically in models with low discretization as illustrated in Figure A1. The front location changing by a factor of 2 between the 50 cell model and the 850 cell model. Due to the lack of a plateau at grid cell dimensions well below a representative elementary volume, the grid discretization of 1,200 cells was chosen because the imbibition front location changed by less than 5% relative to 1,600 cells.

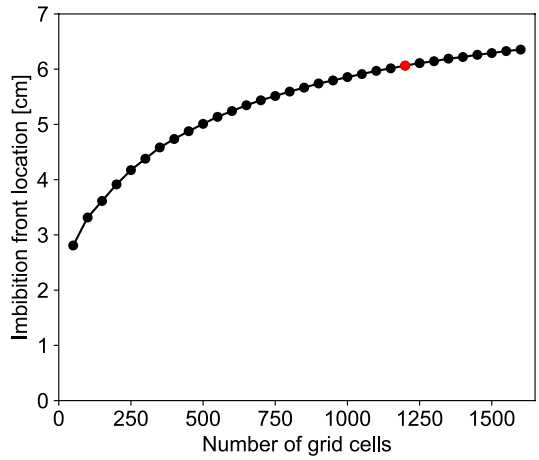

Figure A1. Illustration 1D grid refinement study model results. The black points indicate the imbibition front location after 120 min in a domain with a total length of 10 cm as a function of the number grid cells used to discretize the one-dimensional domain. The red point indicates the discretization that was chosen for the 2D modeling shown in Figure 4.

Appendix B: Capillary Pressure Curve Scaling

The van Genuchten parameters for all grid cell capillary pressure curves in all models were $\lambda = 0.345$, $S_{wr} = 0.03$, $S_{gr} = 1–0.76 = 0.24$, and maximum capillary pressure of 5,000 kPa. The capillary entry pressure was scaled for each layer of the model using the following Levertt-J capillary scaling.

$$P_{i0} = \bar{P}_0 \sqrt{\frac{\bar{k}}{k_i}} \tag{B1}$$

Here, P_{i0} is the layer or grid cell capillary entry pressure, $\bar{P}_0$ is the core-average capillary entry pressure, $\bar{k}$ is the core-average permeability, and k_i is the layer or grid cell permeability. The porosity terms from the classic Levertt-J formulation are neglected due to the approximation of homogeneous porosity. The capillary pressure scaling used for the model with higher capillary heterogeneity is illustrated in Figure B1.

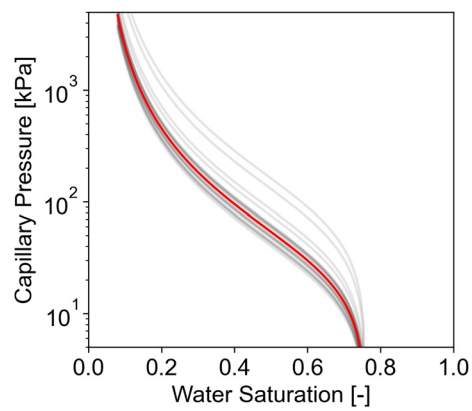

Figure B1. Summary of capillary pressure curves for the model shown in Figure 6 with exaggerated capillary heterogeneity. The core-average capillary pressure curve (red line) is determined from a combination of mercury intrusion capillary pressure measurements (MICP) and 1D numerical capillary pressure calculations using the method of Zahasky and Benson (2019). This core-average capillary pressure curve is identical as that shown in Figure 3. The faint black lines are the scaled capillary pressure curves based on the transformed streamtube permeability (k_{ie}) used in Figure 5.

Data Availability Statement

Datasets, TOUGH2 model input files, and analysis codes are available at Zahasky (2021). The Matlab scripts for the semi-analytical permeability calculation from Zahasky and Benson (2018) are available at Zahasky (2020).

Acknowledgments
This work was supported as part of the Center for Mechanistic Control of Water-Hydrocarbon-Rock Interactions in Unconventional and Tight Oil Formations (CMC-UF), an Energy Frontier Research Center funded by the U.S. Department of Energy, Office of Science under DOE (BES) Award DE-SC0019165. Support for this research was provided by the Global Climate Energy Project, the Stanford Center for Carbon Storage, and the Office of the Vice Chancellor for Research and Graduate Education at the University of Wisconsin-Madison with funding from the Wisconsin Alumni Research Foundation.

References

Akin, S., & Kovscek, A. (2003). Computed tomography in petroleum engineering research. *Applications of X-ray Computed Tomography in the Geosciences*, *215*, 23–38. https://doi.org/10.1144/gsl.sp.2003.215.01.03

Al-Housseiny, T. T., Tsai, P. A., & Stone, H. A. (2012). Control of interfacial instabilities using flow geometry. *Nature Physics*, *8*(10), 747–750. https://doi.org/10.1038/nphys2396

Alyafei, N., Al-Menhali, A., & Blunt, M. J. (2016). Experimental and analytical investigation of spontaneous imbibition in water-wet carbonates. *Transport in Porous Media*, *115*(1), 189–207. https://doi.org/10.1007/s11242-016-0761-4

Alyafei, N., & Blunt, M. J. (2018). Estimation of relative permeability and capillary pressure from mass imbibition experiments. *Advances in Water Resources*, *115*, 88–94. https://doi.org/10.1016/j.advwatres.2018.03.003

Ashraf, S., & Phirani, J. (2019). Capillary displacement of viscous liquids in a multi-layered porous medium. *Soft Matter*, *15*(9), 2057–2070. https://doi.org/10.1039/c8sm02114g

Bartels, W., Rücker, M., Boone, M., Bultreys, T., Mahani, H., Berg, S., et al. (2019). Imaging spontaneous imbibition in full Darcy-scale samples at pore-scale resolution by fast X-ray tomography. *Water Resources Research*, *55*(8), 7072–7085. https://doi.org/10.1029/2018wr024541

Berkowitz, B., Silliman, S. E., & Dunn, A. M. (2004). Impact of the capillary fringe on local flow, chemical migration, and microbiology. *Vadose Zone Journal*, *3*(2), 534–548. https://doi.org/10.2136/vzj2004.0534

Brooks, R. H., & Corey, A. (1966). Properties of porous media affecting fluid flow. *Journal of the Irrigation and Drainage Division*, *92*. https://doi.org/10.1061/JRCEA4.0000425

Debbabi, Y., Jackson, M. D., Hampson, G. J., & Salinas, P. (2017). Capillary heterogeneity trapping and crossflow in layered porous media. *Transport in Porous Media*, *120*(1), 183–206. https://doi.org/10.1007/s11242-017-0915-z

Dogan, M., Van Dam, R. L., Liu, G., Meerschaert, M. M., Butler, J. J., Bohling, G. C., & Hyndman, D. W. (2014). Predicting flow and transport in highly heterogeneous alluvial aquifers. *Geophysical Research Letters*, *41*(21), 7560–7565. https://doi.org/10.1002/2014GL061800

Florian Wellmann, J., Croucher, A., & Regenauer-Lieb, K. (2012). Python scripting libraries for subsurface fluid and heat flow simulations with TOUGH2 and SHEMAT. *Computers & Geosciences*, *43*, 197–206. https://doi.org/10.1016/j.cageo.2011.10.011

Green, C. P., & Ennis-King, J. (2010). Effect of vertical heterogeneity on long-term migration of CO_2 in saline formations. *Transport in Porous Media*, *82*(1), 31–47. https://doi.org/10.1007/s11242-009-9498-7

Gruener, S., Sadjadi, Z., Hermes, H. E., Kityk, A. V., Knorr, K., & Egelhaaf, S. U. (2012). Anomalous front broadening during spontaneous imbibition in a matrix with elongated pores. *Proceedings of the National Academy of Sciences*, *109*(26), 10245–10250. https://doi.org/10.1073/pnas.1119352109

Guo, Y., Holton, C., Luo, H., Dahlen, P., & Johnson, P. C. (2019). Influence of fluctuating groundwater table on volatile organic chemical emission flux at a dissolved chlorinated-solvent plume site. *Groundwater Monitoring and Remediation*, *39*(2), 43–52. https://doi.org/10.1111/gwmr.12322

Hasan, S., Niasar, V., Karadimitriou, N. K., Godinho, J. R., Vo, N. T., An, S., & Steeb, H. (2020). Direct characterization of solute transport in unsaturated porous media using fast X-ray synchrotron microtomography. *Proceedings of the National Academy of Sciences of the United States of America*, *117*(38), 23443–23449. https://doi.org/10.1073/pnas.2011716117

Homsy, G. M. (1987). Viscous fingering in porous media. *Annual Review of Fluid Mechanics*, *19*(1), 271–311. https://doi.org/10.1146/annurev.fl.19.010187.001415

Huang, K., Toride, N., & van Genuchten, M. T. (1995). Experimental investigation of solute transport in large, homogeneous and heterogeneous, saturated soil columns. *Transport in Porous Media*, *18*(1), 283–302. https://doi.org/10.1007/bf00616936

Jackson, S. J., & Krevor, S. (2020). Small-scale capillary heterogeneity linked to rapid plume migration during CO_2 storage. *Geophysical Research Letters*, *41*. https://doi.org/10.1029/2020GL088616

Khan, A. S., Siddiqui, A. R., Abd, A. S., & Alyafei, N. (2018). Guidelines for numerically modeling Co- and counter-current spontaneous imbibition. *Transport in Porous Media*, *124*(3), 743–766. https://doi.org/10.1007/s11242-018-1093-3

Koltermann, C. E., & Gorelick, S. M. (1996). Heterogeneity in sedimentary deposits: A review of structure-imitating, process-imitating, and descriptive approaches. *Water Resources Research*, *32*(9), 2617–2658. https://doi.org/10.1029/96WR00025

Kurotori, T., Zahasky, C., Benson, S. M., & Pini, R. (2020). Description of chemical transport in laboratory rock cores using the continuous random walk formalism. *Water Resources Research*, *56*(9), 1–19. https://doi.org/10.1029/2020wr027511

Kurotori, T., Zahasky, C., Hosseinzadeh Hejazi, S. A., Shah, S. M., Benson, S. M., & Pini, R. (2019). Measuring, imaging and modelling solute transport in a microporous limestone. *Chemical Engineering Science*, *196*, 366–383. https://doi.org/10.1016/j.ces.2018.11.001

Leverett, M. (1940). Capillary behavior in porous solids. *Petroleum Technology*, *142*, 152–169.

Li, B., & Benson, S. M. (2015). Influence of small-scale heterogeneity on upward CO_2 plume migration in storage aquifers. *Advances in Water Resources*, *83*, 389–404. https://doi.org/10.1016/j.advwatres.2015.07.010

Lu, N., Pahlavan, A., Browne, C., Amchin, D., Stone, H., & Datta, S. (2020). Forced imbibition in stratified porous media. *Physical Review Applied*, *14*(5), 054009. https://doi.org/10.1103/PhysRevApplied.14.054009

Lyu, Y., Brusseau, M. L., Chen, W., Yan, N., Fu, X., & Lin, X. (2018). Adsorption of PFOA at the air-water interface during transport in unsaturated porous media. *Environmental Science and Technology*, *52*(14), 7745–7753. https://doi.org/10.1021/acs.est.8b02348

MacMinn, C. W., Neufeld, J. A., Hesse, M. A., & Huppert, H. E. (2012). Spreading and convective dissolution of carbon dioxide in vertically confined, horizontal aquifers. *Water Resources Research*, *48*(11), 1–11. https://doi.org/10.1029/2012WR012286

McCarthy, K. A., & Johnson, R. L. (1993). Transport of volatile organic compounds across the capillary fringe. *Water Resources Research*, *29*(6), 1675–1683. https://doi.org/10.1029/93WR00098

McWhorter, D. B., & Sunada, D. K. (1990). Exact integral solutions for two-phase flow. *Water Resources Research*, *26*(3), 399–413. https://doi.org/10.1029/WR026i003p00399

National Research Council. (2000). *Research needs in subsurface science*. National Academies Press. https://doi.org/10.17226/9793

Pini, R., Krevor, S. C., & Benson, S. M. (2012). Capillary pressure and heterogeneity for the CO_2/water system in sandstone rocks at reservoir conditions. *Advances in Water Resources*, *38*, 48–59. https://doi.org/10.1016/j.advwatres.2011.12.007

Pooladi-Darvish, M., & Firoozabadi, A. (2000). Cocurrent and countercurrent imbibition in a water-wet matrix block. *SPE Journal*, *5*, 3–11. https://doi.org/10.2118/38443-PA

Poulsen, M. M., & Kueper, B. H. (1992). A field experiment to study the behavior of tetrachloroethylene in unsaturated porous media. *Environmental Science and Technology*, *26*(5), 889–895. https://doi.org/10.1021/es00029a003

Pruess, K., & Moridis, G. (2012). *TOUGH2 USER' S GUIDE, VERSION 2 (Tech. Rep. No. November 1999)*.

Rabbani, H. S., Or, D., Liu, Y., Lai, C.-Y., Lu, N. B., Datta, S. S., & Shokri, N. (2018). Suppressing viscous fingering in structured porous media. *Proceedings of the National Academy of Sciences of the USA*, *115*(19), 4833–4838. https://doi.org/10.1073/pnas.1800729115

Ringrose, P. S., Sorbie, K. S., Corbett, P. W., & Jensen, J. L. (1993). Immiscible flow behaviour in laminated and cross-bedded sandstones. *Journal of Petroleum Science and Engineering*, *9*(2), 103–124. https://doi.org/10.1016/0920-4105(93)90071-L

Ross, B. (1990). The diversion capacity of capillary barriers. *Water Resources Research*, *26*(10), 2625–2629. https://doi.org/10.1029/WR026i010p02625

Saffman, P., & Taylor, G. (1958). The penetration of a fluid into a porous medium or Hele-Shaw cell containing a more viscous liquid. *Proceedings of the Royal Society of London*, *A245*, 312–329.

Schlüter, S., Vanderborght, J., & Vogel, H. J. (2012). Hydraulic non-equilibrium during infiltration induced by structural connectivity. *Advances in Water Resources*, *44*, 101–112. https://doi.org/10.1016/j.advwatres.2012.05.002

Silliman, S. E., Berkowitz, B., Simunek, J., & Van Genuchten, M. T. (2002). Fluid flow and solute migration within the capillary fringe. *Ground Water*, *40*(1), 76–84. https://doi.org/10.1111/j.1745-6584.2002.tb02493.x

Tokunaga, T. K., Wan, J., Jung, J. W., Kim, T. W., Kim, Y., & Dong, W. (2013). Capillary pressure and saturation relations for supercritical CO_2 and brine in sand: High-pressure Pc(Sw) controller/meter measurements and capillary scaling predictions. *Water Resources Research*, *49*(8), 4566–4579. https://doi.org/10.1002/wrcr.20316

Vasco, D. W., Pride, S. R., Zahasky, C., & Benson, S. M. (2018). Calculating trajectories associated with solute transport in a heterogeneous medium. *Water Resources Research*, *54*(9), 6890–6908. https://doi.org/10.1029/2018wr023019

Washburn, E. W. (1921). The dynamics of capillary flow. *The Physical Review*, *17*(3), 273–283. https://doi.org/10.1103/PhysRev.17.273

Weber, A. K., Barber, L. B., Leblanc, D. R., Sunderland, E. M., & Vecitis, C. D. (2017). Geochemical and hydrologic factors controlling subsurface transport of poly- and perfluoroalkyl substances, cape cod, Massachusetts. *Environmental Science and Technology*, *51*(8), 4269–4279. https://doi.org/10.1021/acs.est.6b05573

Werner, D., & Höhener, P. (2002). *The influence of water table fluctuations on the volatilization of contaminants from groundwater*. 275, (pp. 213–218). IAHS-AISH Publication. https://doi.org/10.1007/978-3-642-55923-5_10

Woods, A. W. (2014). *Flow in porous rocks: Energy and environmental applications*. Cambridge University Press. https://doi.org/10.1017/CBO9781107588677

Zahasky, C. (2020). *zahasky/streamtube_semianalytical_inversion: Release for Zenodo*. Zenodo. https://doi.org/10.5281/zenodo.3860834

Zahasky, C. (2021). *zahasky/spontaneous_imbibition_analysis: Release for revision*. Zenodo. https://doi.org/10.5281/zenodo.4744460

Zahasky, C., & Benson, S. M. (2018). Micro-positron emission tomography for measuring sub-core scale single and multiphase transport parameters in porous media. *Advances in Water Resources*, *115*, 1–16. https://doi.org/10.1016/j.advwatres.2018.03.002

Zahasky, C., & Benson, S. M. (2019). Spatial and temporal quantification of spontaneous imbibition. *Geophysical Research Letters*, *46*(21), 11972–11982. https://doi.org/10.1029/2019gl084532

Zahasky, C., Jackson, S. J., Lin, Q., & Krevor, S. (2020). Pore network model predictions of Darcy-scale multiphase flow heterogeneity validated by experiments. *Water Resources Research*, *56*, 1–16. https://doi.org/10.1029/2019wr026708

Zahasky, C., Kurotori, T., Pini, R., & Benson, S. M. (2019). Positron emission tomography in water resources and subsurface energy resources engineering research. *Advances in Water Resources*, *127*, 39–52. https://doi.org/10.1016/j.advwatres.2019.03.003

Zhao, Y., Xue, S., Han, S., Chen, Z., Liu, S., Elsworth, D., & Chen, D. (2017). Effects of microstructure on water imbibition in sandstones using X-ray computed tomography and neutron radiography. *Journal of Geophysical Research: Solid Earth*, *122*(7), 4963–4981. https://doi.org/10.1002/2016JB013786